

This is a repository copy of *Filamentary plasma eruptions:Results using the non-linear ballooning model*.

White Rose Research Online URL for this paper:

<https://eprints.whiterose.ac.uk/137548/>

Version: Accepted Version

---

**Article:**

Henneberg, Sophia A., Cowley, Steven C. and Wilson, Howard R. [orcid.org/0000-0003-3333-7470](https://orcid.org/0000-0003-3333-7470) (2018) *Filamentary plasma eruptions:Results using the non-linear ballooning model*. *Contributions to plasma physics*. pp. 6-20. ISSN 0863-1042

<https://doi.org/10.1002/ctpp.201700047>

---

**Reuse**

Items deposited in White Rose Research Online are protected by copyright, with all rights reserved unless indicated otherwise. They may be downloaded and/or printed for private study, or other acts as permitted by national copyright laws. The publisher or other rights holders may allow further reproduction and re-use of the full text version. This is indicated by the licence information on the White Rose Research Online record for the item.

**Takedown**

If you consider content in White Rose Research Online to be in breach of UK law, please notify us by emailing [eprints@whiterose.ac.uk](mailto:eprints@whiterose.ac.uk) including the URL of the record and the reason for the withdrawal request.

## Filamentary plasma eruptions: Results using the nonlinear ballooning model

Sophia A. Henneberg<sup>1,\*</sup>, Steven C. Cowley<sup>2,3</sup>, and Howard R. Wilson<sup>4</sup>

<sup>1</sup> Max-Planck-Institut für Plasmaphysik, Wendelsteinstr. 1, 17489 Greifswald

<sup>2</sup> Rudolf Peierls Centre for Theoretical Physics, University of Oxford, Oxford OX1 3NP, UK

<sup>3</sup> Corpus Christi College, Oxford OX1 4JF, UK

<sup>4</sup> York Plasma Institute, University of York, Dept. of Physics, Heslington, YO10 5DD, UK

Received XXXX, revised XXXX, accepted XXXX

Published online XXXX

**Key words** MHD, nonlinear ballooning model, ELMs

This paper provides an overview of recent results on two distinct studies exploiting the nonlinear model for ideal ballooning modes with potential applications to Edge Localized Modes (ELMs). The nonlinear model for tokamak geometries was developed by Wilson and Cowley in 2004 and consists of two differential equations which characterize the temporal and spatial evolution of the plasma displacement. The variation of the radial displacement along the magnetic field line is described by the first equation, which is identical to the linear ballooning equation. The second differential equation is a two-dimensional nonlinear ballooning-like equation which is often second order in time, but can involve a fractional time derivative depending on the geometry.

In the first study, the interaction of multiple filamentary eruptions is addressed in magnetized plasma in a slab geometry. Equally sized filaments evolve independently in both the linear and nonlinear regime. However, if filaments are initiated with slightly different heights from the reference flux surface, they interact with each other in the nonlinear regime: Lower filaments are slowed down and are eventually completely suppressed while the higher filaments grow faster due to the nonlinear interaction.

In the second study, this model of nonlinear ballooning modes is examined quantitatively against experimental observations of ELMs in MAST geometries. The results suggest experimentally relevant results can only be obtained using modified equilibria.

Copyright line will be provided by the publisher

### 1 Introduction

ITER, the most advanced tokamak, is designed to operate in high-confinement mode (H-mode). This is a desired operational regime for tokamak fusion devices since it has an improved energy confinement time due to an edge transport barrier. This, however, creates a steep pressure gradient which can trigger so-called Edge Localized Modes (ELMs).

ELMs are quasi-periodic instabilities which grow very rapidly radially outwards and release a substantial amount of energy onto the plasma facing components if not controlled. Therefore ELMs represent a major challenge for future tokamak fusion devices. The leading theory for determining the stability condition of the Type I ELMs is the peeling-ballooning model [1–3]. It unites the boundaries of two instabilities: ballooning instability and the peeling instability, [1, 4]. These modes are driven by different physical mechanisms; the ballooning instability is typically driven by a pressure gradient in combination with an unfavorable direction of the curvature and peeling modes are typically driven by the edge current density and stabilized by the edge pressure gradient.

In addition to determining stability, one would like to simulate the evolution of ELMs. The nonlinear ballooning theory describes the early nonlinear evolution of explosive filaments and is therefore a good model for examining the dynamics of ELMs. Hurricane et.al. [5] described the filamentary eruptions with the the nonlinear ballooning approach, but for generalized magnetic field geometries. In 2003 the nonlinear envelope equation for some toroidal cases was derived by Cowley et.al [6], which mentioned the potential application for ELMs. Wilson and Cowley [7] continued these calculations for a more complete tokamak geometry and presented the nonlinear

---

\*Corresponding author E-mail: Sophia.Henneberg@mpg.ipp.de, Phone: +49 3834 88 1284

ballooning differential equations for tokamaks. In [8] (or for more details [9]) there is a more detailed description of how filaments behave in plasmas including the nonlinear ballooning model with an additional scalar viscosity term. How filaments with different initial sizes interact with each other has also been investigated [10]. This model has correctly described several qualitative aspects of ELMs [11–13], including the relatively long inter-ELM time compared to explosive growth of ELMs; their filamentary structure, which was correctly predicted by the nonlinear ballooning model [14]; and the large spacing between ELM filaments compared to the filament widths.

To allow, however, a quantitative comparison between this nonlinear ballooning theory and experiments (e.g. ELMs) one must evaluate the coefficients of the nonlinear ballooning equation for tokamak geometries [15, 16].

In the first part of this paper, a summary of the work on the interaction of filaments with slightly altered initial amplitudes is presented. In the second part, we summarize results of the nonlinear ballooning model using a Type I ELMy MAST equilibrium.

## 2 Nonlinear interaction of filamentary eruptions

In this section an overview of the interaction of multiple filamentary plasma eruptions is presented. This is investigated by modelling the nonlinear MHD ballooning mode envelope equation in a specific slab equilibrium susceptible to Rayleigh-Taylor instabilities as employed in [8, 17].

### 2.1 Theoretical model

First, we outline the derivation of the nonlinear equation for the slab Rayleigh-Taylor model using boundary conditions that forbid vertical plasma displacements and perturbed density or pressure at the walls.

The equilibrium analyzed is of a simple one dimensional line tied magnetized plasma atmosphere. It is described by a magnetic field  $\mathbf{B}_0 = B_0(x) \hat{z}$ , the pressure  $p_0 = p_0(x)$ , the density  $\rho_0 = \rho_0(x)$  and the gravitational acceleration  $\mathbf{g} = -g \hat{x}$ , as shown in Fig. 1. Equilibrium quantities are denoted by the zero subscript. The derivation starts with the ideal MHD momentum equation allowing for gravitational effects and with an additional kinematic, scalar viscosity ( $\nu$ ) term that is inserted to provide simple viscous dissipation [18]:

$$\rho \left( \frac{\partial \mathbf{v}}{\partial t} + \mathbf{v} \cdot \nabla \mathbf{v} \right) = -\nabla \left( p + \frac{B^2}{2} \right) + \mathbf{B} \cdot \nabla \mathbf{B} - \rho g \hat{x} + \nu \rho \nabla^2 \mathbf{v}. \quad (1)$$

where  $\mathbf{v} = \frac{\partial \mathbf{r}}{\partial t}$  is the velocity. The calculation is performed in Lagrangian variables with which all quantities can be expressed in terms of the displacement  $\xi$  of a fluid element. The displacement expresses how far fluid elements

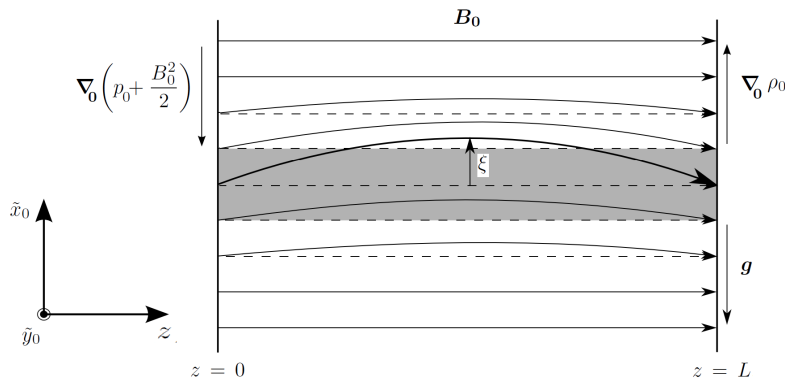


**Fig. 1** Equilibrium (dashed field lines) and slightly perturbed system (curved field lines) are shown. The displacement  $\xi$  denotes how much the magnetic field lines or filaments have evolved from the equilibrium position. The gravity  $g$  is pointing downwards and a density gradient is pointing upwards which results in a Rayleigh-Taylor drive. In the equilibrium case this drive is balanced by the pressure and magnetic field gradient.

have moved from their initial position  $\mathbf{r}_0$  and one can represent the current position as:  $\mathbf{r}(t) = \mathbf{r}_0 + \boldsymbol{\xi}(\mathbf{r}_0, t)$ . The components of the Jacobian matrix  $J_{ij}$  of this transformation are

$$J_{ij} = (\nabla_0 \mathbf{r})_{ij} = \delta_{ij} + \frac{\partial \xi_j}{\partial x_{0i}}, \quad (2)$$

where  $x_{0i}$  are the components of  $\mathbf{r}_0$ ;  $i, j$  stand for  $x, y$  or  $z$  coordinates of a Cartesian system, and  $J$  is the determinant of the Jacobian matrix  $J_{ij}$ . The boundary conditions of unperturbed pressure  $p$  and density  $\rho$  can now be expressed as  $\xi_x = 0$  and  $J = 1$  at the walls which are at  $z = 0$  and  $z = L$ . We suppose that gradients in the  $\rho$  and  $p$  profiles are in the  $x$ -direction and that the thermal conduction along the field lines is fast, which implies that the process is isothermal.

To enforce a ballooning like evolution, we introduce an ordering parameter  $n$ . We measure the distance above marginal stability by this dummy large parameter  $n$ , where the growth rate of the most unstable perturbation  $\Gamma$  is order  $n^{-1/2}$ . Thus

$$\frac{\partial}{\partial t} \sim \mathcal{O}(n^{-1/2}) \quad (3)$$

The order of the spatial derivatives as well as the order of the Lagrangian displacement is set by the localised geometry of the most unstable linear mode structure [17] which is similar to the ballooning mode structure [19]:

$$\frac{\partial}{\partial x_0} \sim \mathcal{O}(n^{+1/2}) \quad k_y \sim \frac{\partial}{\partial y_0} \sim \mathcal{O}(n) \quad \frac{\partial}{\partial z_0} \sim \mathcal{O}(1). \quad (4)$$

The next step is to expand the components of  $\boldsymbol{\xi} = \xi_x \hat{\mathbf{x}} + \xi_z \hat{\mathbf{z}} + \xi_y \hat{\mathbf{y}}$  and the Jacobian  $J$  in powers of  $n^{-1/2}$ . We anticipate:

$$\xi_x = \sum_{i=2}^{\infty} n^{-i/2} \xi_x^{(i/2)} \quad \xi_z = \sum_{i=2}^{\infty} n^{-i/2} \xi_z^{(i/2)} \quad \xi_y = \sum_{i=3}^{\infty} n^{-i/2} \xi_y^{(i/2)} \quad J = 1 + \sum_{i=1}^{\infty} n^{-i/2} J^{(i/2)}. \quad (5)$$

The viscosity is treated as small  $\nu \sim \mathcal{O}(n^{-5/2})$  so that it only enters in our envelope equation for  $\xi_x$ . The derivation includes analyzing the different orders of  $n$  of the  $x_0$ -component and the  $y_0$ -component of the Lagrangian MHD momentum equation. This derivation is a simplified version of the one for tokamak geometry [7] due to its boundary conditions and the simpler geometry. Nevertheless one still must evaluate up to fifth order to obtain the final equation. The full calculation is reported in [16] which derives the following equation for the evolution of filaments in the direction perpendicular to the magnetic field lines:

$$\begin{aligned} \text{Inertia Term} & \quad \hat{C}_0 \frac{\partial^2 \xi}{\partial t^2} & = & \quad \text{Linear Instability Drive} & \quad \text{Field Line Stability Term} & \quad \text{Viscosity Term} \\ & & & \quad \Gamma^2(x_0) \xi & \quad - \hat{C}_2 \frac{\partial^2 u}{\partial x_0^2} & \quad + \nu \frac{\partial^2}{\partial y_0^2} \frac{\partial \xi}{\partial t} \\ & & & + \hat{C}_3 \xi \frac{\partial^2 \bar{\xi}^2}{\partial x_0^2} & + \hat{C}_4 (\xi^2 - \bar{\xi}^2) & \\ & & & \text{Quasilinear Nonlinearity Term} & \text{Nonlinear Growth Drive} & \end{aligned} \quad (6)$$

Here we have  $\xi_x(x_0, y_0, z_0) = \xi(x_0, y_0, t)H(z)$  where the function  $H(z)$  describes the vertical displacement along the field line:  $H(z) = \sin(\frac{\pi z}{L})$ . We have also defined  $\bar{\xi}^2$  as the  $y_0$  average of the squared displacement,  $\bar{\xi}^2$  and  $\frac{\partial^2 u}{\partial y_0^2} = \xi$ . The local linear growth rate  $\Gamma$  is given by, [9]:

$$\Gamma^2(x_0) = -\frac{B_0^2 \pi^2}{\rho_0 L^2} + \frac{\rho_0 g^2}{p_0} + \frac{g}{\rho_0} \frac{d\rho_0}{dx_0}. \quad (7)$$

The first term describes the stabilising effect of field line bending, the second term is the Parker instability drive and the third term is the Rayleigh-Taylor instability drive.

The coefficients  $\hat{C}_0$ ,  $\hat{C}_2$ ,  $\hat{C}_3$  and  $\hat{C}_4$  are given by:

$$\begin{aligned}\hat{C}_0 &= \left(1 + \frac{\rho_0^2 g^2 L^2}{p_0^2 \pi^2}\right) & \hat{C}_2 &= -\left(\frac{B_0^2 \pi^2}{\rho_0 L^2}\right) \\ \hat{C}_3 &= \left(\frac{B_0^2 \pi^2}{8 \rho_0 L^2}\right) & \hat{C}_4 &= \frac{4}{3\pi} \left(\frac{g}{\rho_0} \frac{d^2 \rho_0}{dx_0^2} - \frac{\rho_0^2 g^3}{p_0^2}\right)\end{aligned}\quad (8)$$

Notice that Eq. (6) has the same form as the one for tokamak geometry presented in [7] except that it always has a second time derivative instead of a fractional time derivative. This is one reason why the results shown here are generic and are considered to be relevant for tokamak geometry especially in cases with strong shaping [7].

## 2.2 A model equilibrium

We calculate coefficients for a simple model atmosphere in a slab geometry, which is an extension of that used in [9]. The equilibrium density and magnetic field are chosen to be:

$$\rho(x_0) = \frac{\bar{\rho}}{\cosh^2 \left[ \frac{x_0 - x_\rho}{L_\rho} \right]} \quad B_0^2(x_0) = \bar{B}_1^2 - \frac{\bar{B}_2^2}{\cosh^2 \left[ \frac{x_0 - x_E}{L_\rho} \right]}.\quad (9)$$

From the equilibrium equation  $\frac{\partial}{\partial x} \left( p_0 + \frac{B_0^2}{2} \right) = -g\rho_0$  we obtain the following for the equilibrium pressure profile:

$$p_0(x_0) = \bar{p}_0 - \frac{B_0^2}{2} - g\bar{\rho}_0 L_\rho \tanh \left[ \frac{x_0 - x_\rho}{L_\rho} \right].\quad (10)$$

Similar to [9], we define normalised variables and constants:

$$\begin{aligned}\tilde{x}_0 &= \frac{x_0}{L_\rho}, & \tilde{y}_0 &= \frac{y_0}{L_\rho}, & \tilde{t} &= \sqrt{\frac{g}{L_\rho}} t, & \tilde{B}_1^2 &= \frac{\bar{B}_1^2}{2g\bar{\rho}_0 L_\rho}, & \tilde{\xi} &= \frac{\xi}{L_\rho}, \\ \tilde{x}_B &= \frac{x_B}{L_\rho}, & \tilde{x}_\rho &= \frac{x_\rho}{L_\rho}, & A &= \frac{L_\rho}{L}, & \tilde{B}_2^2 &= \frac{\bar{B}_2^2}{2g\bar{\rho}_0 L_\rho}.\end{aligned}$$

We transform the coefficients in Eq. (6) such that this equation maintains its form:

$$\tilde{C}_0 = \hat{C}_0 \frac{\rho_0}{2\bar{\rho}} \quad \tilde{C}_3 = \hat{C}_3 \frac{L_\rho \rho_0}{2g\bar{\rho}} \quad (11)$$

$$\tilde{\Gamma}^2 = \Gamma^2 \frac{L_\rho \rho_0}{2g\bar{\rho}} \quad \tilde{C}_4 = \hat{C}_4 \frac{L_\rho^2 \rho_0}{2g\bar{\rho}} \quad (12)$$

$$\tilde{C}_2 = \hat{C}_2 \frac{L_\rho \rho_0}{2g\bar{\rho}} \quad \tilde{\nu} = \nu \frac{\rho_0}{2\bar{\rho} \sqrt{gL_\rho^3}} \quad (13)$$

With these expressions we obtain:

$$\tilde{C}_0 \frac{\partial^2 \tilde{\xi}}{\partial \tilde{t}^2} = \tilde{\Gamma}^2(\tilde{x}_0) \tilde{\xi} - \tilde{C}_2 \frac{\partial^2 \tilde{u}}{\partial \tilde{x}_0^2} + \tilde{C}_3 \tilde{\xi} \frac{\partial^2 \tilde{\xi}^2}{\partial \tilde{x}_0^2} + \tilde{C}_4 (\tilde{\xi}^2 - \tilde{\xi}^2) + \tilde{\nu} \frac{\partial^2}{\partial \tilde{y}_0^2} \frac{\partial \tilde{\xi}}{\partial \tilde{t}} \quad (14)$$

where  $\frac{\partial^2 \tilde{u}}{\partial \tilde{y}_0^2} \equiv \tilde{\xi}$ . To derive the normalised coefficients  $\tilde{C}_i$  we use equations (8) and assume a large pressure to ensure that the Rayleigh-Taylor instability dominates over the Parker instability drive. We then obtain:

$$\begin{aligned}\tilde{\Gamma}^2(\tilde{x}_0) &= - \left( A^2 \tilde{B}_1^2 - \frac{A^2 \tilde{B}_2^2}{\cosh^2(\tilde{x}_0 - \tilde{x}_B)} \right) \pi^2 - \frac{\sinh(\tilde{x}_0 - \tilde{x}_\rho)}{\cosh^3(\tilde{x}_0 - \tilde{x}_\rho)} \\ \tilde{C}_0 &= \frac{\rho_0}{2\bar{\rho}_0} = \frac{1}{2 \cosh^2(\tilde{x}_0 - \tilde{x}_\rho)} \\ \tilde{C}_2 &= - \frac{L_\rho}{2g\bar{\rho}_0} \left( \frac{B_0^2 \pi^2}{L^2} \right) = - \left( A^2 \tilde{B}_1^2 - \frac{A^2 \tilde{B}_2^2}{\cosh^2(\tilde{x}_0 - \tilde{x}_B)} \right) \pi^2 \\ \tilde{C}_3 &= \frac{L_\rho}{16g\bar{\rho}_0} \left( \frac{B_0^2 \pi^2}{L^2} \right) = \frac{1}{8} \left( A^2 \tilde{B}_1^2 - \frac{A^2 \tilde{B}_2^2}{\cosh^2(\tilde{x}_0 - \tilde{x}_B)} \right) \pi^2 \\ \tilde{C}_4 &= \frac{2L_\rho^2}{3\pi\bar{\rho}_0} \frac{d^2 \rho_0}{dx_0^2} = \frac{8}{3\pi} \frac{3 \tanh^2(\tilde{x}_0 - \tilde{x}_\rho) - 1}{\cosh^2(\tilde{x}_0 - \tilde{x}_\rho)}.\end{aligned}$$

The linear drive coefficient  $\tilde{\Gamma}^2(x_0)$  can be expanded about the position  $x_{max}$  where the growth rate has a maximum:

$$\begin{aligned}\tilde{\Gamma}^2(x_0) &\approx \tilde{\Gamma}^2(x_{max}) - \left. \frac{d\tilde{\Gamma}^2}{dx_0^2} \right|_{x_{max}} \left( \frac{(x_0 - x_{max})^2}{2} \right) \\ &= \tilde{C}_1 \left( 1 - \frac{(\tilde{x}_0 - \tilde{x}_{max})^2}{\Delta^2} \right)\end{aligned}\tag{15}$$

We adopt the same choice of variables as Ref. [9] to enable comparison:  $\tilde{x}_\rho = 2$ ,  $\tilde{x}_B = 0.8$ ,  $A^2 \tilde{B}_1^2 = 0.07834$  and  $A^2 \tilde{B}_2^2 = 0.04701$ . With these parameters we obtain:

$$\begin{aligned}\tilde{C}_0 &= 0.248 & \tilde{C}_1 &= 1.9 \times 10^{-4} & \tilde{C}_2 &= -0.352 \\ \tilde{C}_3 &= 0.044 & \tilde{C}_4 &= 0.216 \\ \Delta &= 0.017 & \tilde{x}_{max} &= 1.1118\end{aligned}$$

and we chose the viscosity to be  $\bar{\nu} = 10^{-10}$ . The effects of this small scale viscosity are presented in [9, 16]. In summary the small viscosity influences the nonlinear evolution as it determines the behavior of the width of the filaments in both perpendicular directions in the nonlinear regime. However, the viscosity chosen here has only a minor impact on the evolution.

### 2.3 Initiation - linear solution

A linear stability analysis of Eq. (6) (Neglecting the last two terms of Eq. (6)) provides an eigenmode structure of the displacement which can be used to initialize the simulations. To solve the linear differential equation, one can use a separation of variables:

$$\xi = X(x_0) Y(y_0) T(t)\tag{16}$$

Using the ansatz that  $Y(y_0) = \cos(ny_0)$  and  $T(t) = \exp(\gamma t)$ , where  $n$  is the mode number and  $\gamma$  the linear growth rate, one obtains a Weber differential equation for the  $x_0$  component [20]:

$$\frac{C_2}{n^2} \frac{\partial^2 X(x_0)}{\partial x_0^2} + \left[ C_0 \gamma^2 + n^2 \nu \gamma - C_1 \left( 1 - \frac{(x_0 - x_{max})^2}{\Delta^2} \right) \right] X(x_0) = 0\tag{17}$$

Its solution is a Gaussian function:  $X(x_0) = \exp(-\frac{x_0^2}{2\sigma^2})$ . Combining, we initialize the displacement  $\xi$  with  $\xi(x_0, y_0, t = 0) = h \cos(ny_0) e^{-\frac{x_0^2}{2\sigma^2}}$  where the Gaussian width  $\sigma^2(n) = \frac{4\Delta}{n} \sqrt{\frac{|C_2|}{C_1}}$  and a linear growth rate

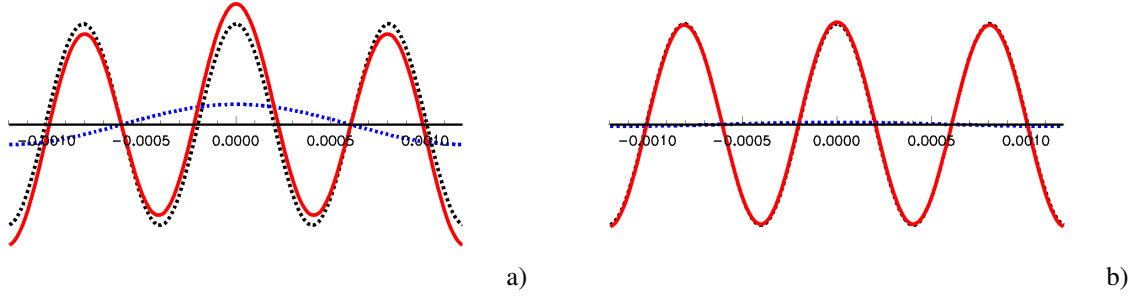


**Fig. 2** Initiation of the filaments for two different choices of relative amplitude: **a)** Superposition (red) of two modes with  $n_2 = 3n_1$  and  $h_2 = 5h_1$ . Blue:  $n_1$  and black  $n_2$ -mode. In the middle is the main central filament with two side filaments. **b)** Superposition (red) of two modes. This time with the actual heights  $h_2 = 50h_1$  which produces a less than 2% larger main filament.

$$\gamma(n) = -\frac{n^2\nu}{2C_0} + \sqrt{\frac{C_1}{C_0} - \frac{\sqrt{C_1|C_2|}}{C_0n\Delta} + \frac{n^4\nu^2}{4C_0^2}}.$$

$h$  is an arbitrary constant which has to be chosen sufficiently small so that the linear terms of Eq. (6) are dominant. To explore the nonlinear evolution predicted by Eq. (6) we initialize the system at  $t = 0$  with the linear eigenmode and evolve in time. As we wish to explore how filaments of different heights evolve in time we initialize four distinct systems with

1. a superposition of two linear eigenmodes, with two mode numbers  $n_1, n_2$  and two heights  $h_1$  and  $h_2$ :

$$\xi_{\text{init}} = h_1 \cos(n_1 y_0) e^{(-\sigma_1 x_0^2 + \gamma_1 t)} + h_2 \cos(n_2 y_0) e^{(-\sigma_2 x_0^2 + \gamma_2 t)}, \quad (18)$$

2. a single mode with the mode number  $n_1$  and height  $h_1$ ,
3. a single mode with the mode number  $n_2$  and height  $h_2$ ,
4. and a single mode with the mode number  $n_2$  and the height  $h = h_1 + h_2$ .

Case 1 is the new case we are mainly interested in. Cases 2 and 3 are simulated to identify when the nonlinear regime is starting, and how the nonlinear interaction changes the behavior. Case 4 is used to show how the interaction changes the behavior compared to a case where the tallest filaments have the same heights, to exclude that as the reason why the main filament grows faster.

#### Case 1: A superposition of two linear eigenmodes:

If we select  $n_2 = 3n_1$ , this provides a perturbation which repeats every three oscillations in the  $y_0$ -direction. Thus, our simulation domain in this direction needs to contain only three oscillations, or filaments. If we take  $h_1 = 0$ , all three filaments will initially have the same amplitude (i.e.  $h_2$ ). By introducing a small amount of  $h_1$ , we can enhance the initial amplitude of the central filament compared to the two side filaments. We select  $n_1 = 2600$  and  $n_2 = 7800$  which have linear growth rates  $\gamma_1 = 0.0033$  and  $\gamma_2 = 0.0136$ . This ensures that the linear evolution reinforces the three filaments, so any deviation from this must be a nonlinear effect.

We initiate our perturbation with  $h_2 = 50h_1$  which ensures the filaments are initially very close in amplitude, but the central one penetrates slightly further than the two side filaments, see Fig. 2.

#### Case 2 and 3: two single mode initiations

All parameters are chosen as in the first case, but the two cases are simulated separately rather than superimposed. Therefore case 2 has  $n = n_1$  and  $h = h_1$ , (see the blue line in Fig 2 **b**) ) and case 3 has  $n = n_2$  and  $h = h_2$  (see the black line in Fig. 2 **b**) ).

#### Case 4: another single mode

Here we chose the mode number and the height so that the mode is the same as the dominant mode in case 1 but also the height is the same as the largest filament in case 1:  $n = n_2$  and  $h = h_1 + h_2$ .

## 2.4 The evolution of multiple filaments

We can show that the energy of each term is described by the following expression where the dissipated energy is equal to the viscosity term on the right hand side:

$$\begin{aligned} 2\frac{dE}{dt} &= \frac{d}{dt} \int dV \left[ C_0 \left( \frac{\partial \xi}{\partial t} \right)^2 - \Gamma^2 \xi^2 + C_2 \left( \frac{\partial u}{\partial x_0} \right)^2 + \frac{1}{2} C_3 \left( \frac{\partial \xi^2}{\partial x_0} \right)^2 - \frac{2}{3} C_4 \xi^3 \right] \\ &= -\nu \int dV \left( \frac{\partial^2 \xi}{\partial t \partial y_0} \right)^2 \end{aligned} \quad (19)$$

where  $\int dV = \int dx_0 dy_0 L_z$  is a volume integral. The dominant terms originated from the inertia  $C_0$  and from the explosive nonlinear term  $C_4$  of Eq. (6). A standard estimate for the onset of the nonlinear regime is the time when the energy of the quadratic nonlinear drive term exceeds the energy of the linear drive term. From Fig. 3 we can evaluate this time to be  $t \approx 260$ .

Through comparing the results of the simulations of the filaments of case 1 and case 3 we find that the main filament grows faster than in the single filament case. To explore this further, we investigate the height of the main filament with respect to the ‘‘ground level’’ because this ground level is always reduced in the nonlinear regime in the scope of this model [17]. The reasons for this is presented later. Thus we define  $H_{mf}(t) = \xi(x_0 = x_{max}, y = 0.0, t) - \min(\xi(x_{max}, y, t))$ , see Fig. 4. The height of the side filament is defined in an equivalent manner. Evaluating the evolution of the two heights (see Fig. 5) one can clearly determine the linear and nonlinear phases and the time of the transition of the two which is consistent with the energy consideration. In the linear phase the side and main filaments grow equally. However, when the main filament enters the nonlinear regime the evolution starts to diverge such that the main filament grows stronger and eventually the side filament slows down and diminishes in size until it is fully suppressed. Comparing not only one flux surface but an entire set (Fig. 6) one can discover that the side filaments evolve towards different values of  $x_0$  away from the most unstable flux surface denoted by  $x_{max}$ .

To evaluate the solution of the combined modes with the sum of the two individual mode solution, case 2 and 3, we define

$$\Delta \xi = \xi_{n_1+n_2} - (\xi_{n_1} + \xi_{n_2}). \quad (20)$$

Here  $\xi_{n_1+n_2}$  is the displacement of case 1 and  $\xi_{n_1}$  and  $\xi_{n_2}$  are the solutions from case 2 and case 3, respectively. We are expecting  $\Delta \xi$  to be nearly zero at the beginning of the evolution when the linear terms dominate as the modes evolve independently since they satisfy the superposition principle:  $F(\sum_i x_i) = \sum_i F(x_i)$ , where  $F$

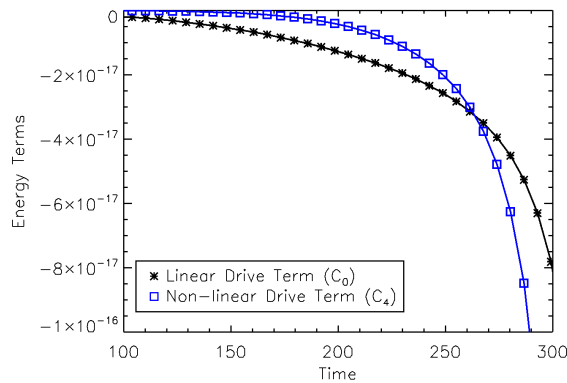


**Fig. 3** Energies of the linear  $C_0$  (black, \*-symbols) drive term and the quadratic nonlinear  $C_4$  (blue, □-symbols) drive term are shown. The absolute value determines which mechanism drives the evolution. The linear term drives the evolution first and then the nonlinear drive takes over. [10]

represents the solution of the differential equation and  $x_i$  are different initializations. As the plasma enters the nonlinear regime the superposition of the modes will deviate from the sum of the two distinct solutions. We are interested in how the interaction between the two modes changes their evolution. To explore this we examine  $\Delta\xi$ , as shown in Fig. 7. Positive values of  $\Delta\xi$  imply that the coupled filaments grow further than the sum of the two individual modes and negative values of  $\Delta\xi$  mean that they grow slower. In Fig. 7 we show the spatial structure of  $\Delta\xi$  deep inside the nonlinear phase. The main filament is indicated by the positive  $\Delta\xi$  peak, and clearly grows stronger, suppressing the two side filaments for which  $\Delta\xi < 0$ .

To normalize this change with respect to case 1, we define the interaction coefficient  $p_i = \frac{\Delta\xi}{\xi_{n_1+n_2}}$  for the main filament, which characterizes the fraction of the main filament height due to the coupling to the side filaments. In the linear phase  $p_i$  is also approximately zero, as expected, however, deep in the nonlinear regime, at  $t = 370$ , the height of the main filament is over 80 % due to the interaction with the side filaments.

The mathematical origin of this behavior can be comprehended by analyzing the nonlinear ballooning equation. The dominant terms which determine the evolution in the nonlinear regime are the quasilinear nonlinearity term and the nonlinear growth drive term. Both terms are composed of a contribution of  $\xi^2$  which is an average of  $\xi^2$

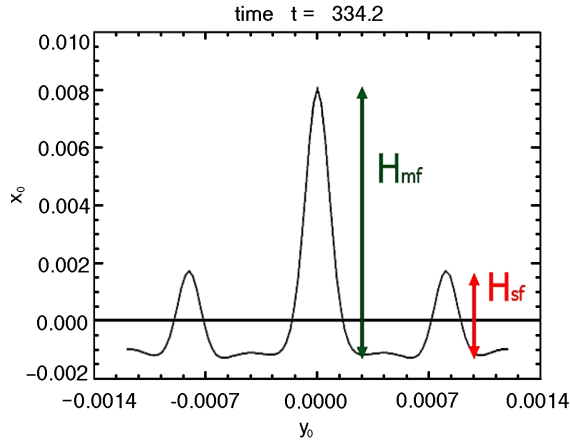


**Fig. 4** The main filament height  $H_{mf}$  and the side filament height  $H_{sf}$  on the most unstable flux line is plotted. Note how the "ground level" is reduced compared to zero – the equilibrium location of this flux surface.

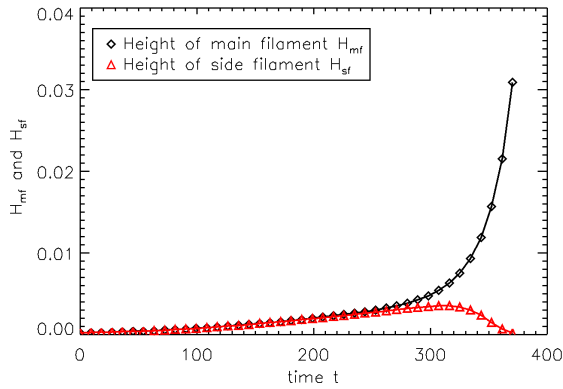


**Fig. 5** The temporal evolution at  $x_0 = x_{max}$  of the main filament  $H_{mf}$  (black,  $\diamond$ -symbol) and the side filament  $H_{sf}$  (red,  $\triangle$ -symbol) [10]

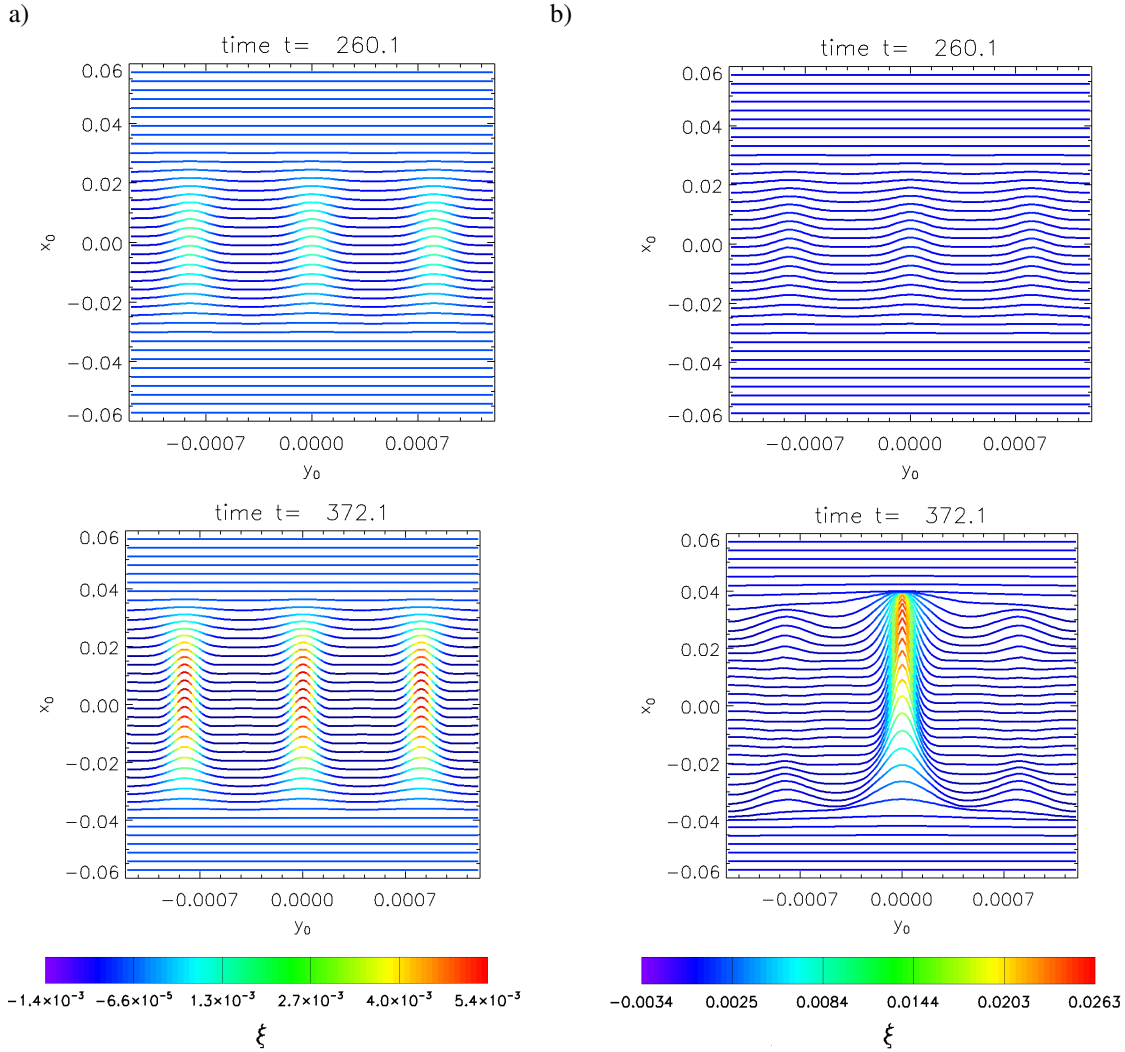


**Fig. 6** The flux surfaces in the  $x$ - $y$  plane at  $z = L/2$  (half way between the plates). The color visualizes the displacement. The top is at the beginning of the nonlinear regime  $t \approx 260$ . The bottom shows the end of the simulation at  $t = 370$ , which is deep in the nonlinear regime, just as the perturbed flux surfaces of case 1 are about to overtake each other: **a)** Initialized with three equal sized filaments (case 4). **b)** Central, main filament is initialized slightly larger (less than 2%) than the two side filaments (case 1). At the later time the two side filaments are much smaller than the main central filament and the amplitude of the main filament is approximately 5 times larger than in case 4.

with respect of the  $y_0$  direction. Once one filament enters the nonlinear regime it grows explosively and dominates  $\bar{\xi}^2$ . At this location the nonlinear growth drive term  $C_4 (\xi^2 - \bar{\xi}^2)$  will be positive as  $\xi^2 > \bar{\xi}^2$ . Everywhere else  $\xi^2 < \bar{\xi}^2$  which causes the side filaments to be suppressed and the ground level to be reduced. The second nonlinear  $C_3$  term consists of  $C_3 \xi \frac{\partial^2 \bar{\xi}^2}{\partial x_0^2}$  where the second derivative is pictured in Fig. 8. It is negative at the most unstable flux surface and therefore serves as a damping term. However, further away from the most unstable location  $\frac{\partial^2 \bar{\xi}^2}{\partial x_0^2}$  reverses its sign and leads to a drive in the positive  $x_0$  direction. This explains the remnants of the side filaments further away from the most unstable flux surface, Fig. 6.

Consequently, one can conclude the physical mechanism from the mathematical description. The  $\bar{\xi}^2$  arises in the derivation of the nonlinear ballooning model as a consequence of a leading order incompressibility characteristic of the plasma. As the main filament enters the nonlinear regime it explosively grows and would compress

the plasma on top. Due to the incompressibility this plasma instead flows down on both sides of the main filament causing a down-draft which suppresses the side filaments.

### 2.5 Experimental observation

There exists experimental observations which may be described by our simulations presented here. We present two selected examples: type V ELMs in the NSTX tokamak [21] and ELMs in KSTAR [22]. The small, type V ELMs in NSTX involve fine-scale filaments that one would typically associate with higher toroidal mode number  $n$ . However, these ELMs only consist of one or two filaments which is in disagreement with what one would expect,  $\sim n$  filaments, from linear theory. While experimental evidence indicates the dominant instability drive is current density rather than ballooning modes, it is possible that a similar mechanism to that identified here acts to limit the number of filaments.

Another example which might be described by the nonlinear ballooning mode with interacting filaments are ELMs in KSTAR [22]. They observe slowly growing “fingers” out of the plasma which at some point suddenly transforms into a more irregular formation followed by apparent suppression of filaments, which could be explained by the results presented here.

## 3 Type I ELMs in a MAST equilibrium

In this section a MAST Type I ELMy H-mode equilibrium is investigated (shot 24763). The fits of the profiles were produced by the standard equilibrium reconstruction code EFIT [23] and the equilibrium was calculated with the fixed boundary equilibrium solver HELENA which solves the Grad-Shafranov equation [24, 25].

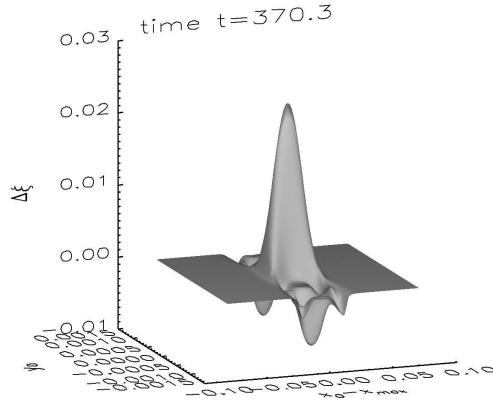


**Fig. 7** The spatial structure of  $\Delta\xi$  deep in the nonlinear regime. Note the holes at the position of the side filaments which indicate that they get “eaten” by the main-filament.

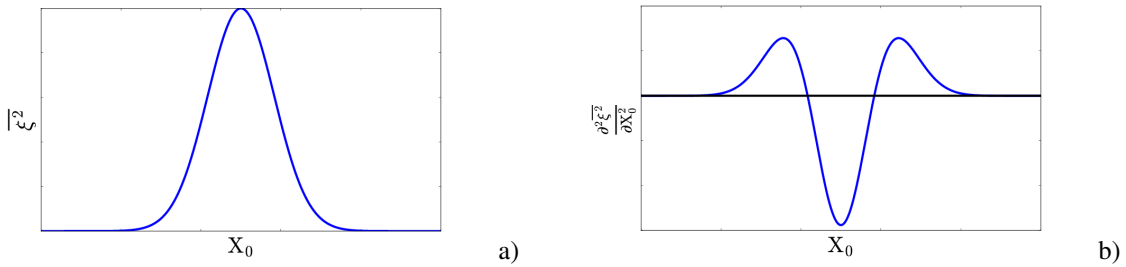


**Fig. 8** **a)** Sketch of  $\xi^2$  profile versus  $x_0$  which has a similar shape to a Gaussian. **b)** Sketch of  $\frac{\partial^2 \xi^2}{\partial \psi^2}$  profile which is of a similar form of the second derivative of a Gaussian.

### 3.1 Nonlinear ballooning model for Tokamak geometries

To account for the tokamak geometry the Clebsch coordinate system is utilized where the magnetic field is written as [26]:

$$\mathbf{B}_0 = \nabla\psi \times \nabla\alpha \quad (21)$$

where  $\alpha$  labels the magnetic field lines on a certain flux surface  $\psi$  and  $\alpha$  is chosen to be:

$$\alpha = q(\psi)\theta - \phi \quad (22)$$

where  $\phi$  is the toroidal angle,  $\theta$  is the poloidal angle in straight field line coordinates and  $q$  is the safety factor which describes how many times a certain magnetic field line goes around the torus for one poloidal revolution. So far we have only chosen two variables for the Clebsch coordinate:  $\psi$  and  $\alpha$ . The third one can be chosen freely. Here we choose it as a poloidal angle  $\chi$  which increases by  $2\pi$  each time a field line goes around poloidally. We generate new basis vectors:  $e_\perp$ ,  $e_\wedge$  and  $\mathbf{B}_0$  to decompose the quantities into perpendicular and parallel components relative to the magnetic field line. The first two vectors are defined as:

$$\mathbf{e}_\perp \equiv \frac{\nabla\alpha \times \mathbf{B}_0}{B_0} \quad (23)$$

$$\mathbf{e}_\wedge \equiv \frac{\mathbf{B}_0 \times \nabla\psi}{B_0} \quad (24)$$

$\mathbf{e}_\perp$  and  $\mathbf{e}_\wedge$  are vectors perpendicular to the equilibrium magnetic field lines  $\mathbf{B}_0$ . The leading order displacement can be again separated in the following way:

$$\boldsymbol{\xi}^{(2)} = \xi(\psi, \alpha; t) \left[ \frac{X}{B_0} \mathbf{e}_\perp + G \mathbf{B}_0 \right] = \xi(\psi, \alpha; t) \mathbf{H} \quad (25)$$

where  $\mathbf{H}$  is defined as:  $\mathbf{H} \equiv \frac{X}{B_0} \mathbf{e}_\perp + G \mathbf{B}_0$ . The ratio  $\frac{X}{B_0}$  is independent of a fast variation of  $\psi$ ,  $\alpha$  and  $t$  and is determined by the linear ballooning equation [19]:

$$(\mathbf{B}_0 \cdot \nabla_0) \left[ \frac{|\mathbf{e}_\perp|^2}{B_0^2} (\mathbf{B}_0 \cdot \nabla_0) X \right] + \frac{2\mu}{B_0^4} (\mathbf{e}_\perp \cdot \boldsymbol{\kappa}_0) (\mathbf{e}_\perp \cdot \nabla_0 p_0) X = 0 \quad (26)$$

where  $\mu$  is the so called ballooning eigenvalue. The equation describing the parallel component of  $\boldsymbol{\xi}^{(2)}$  is:

$$G = -\frac{1}{\mu p_0} \frac{|\mathbf{e}_\perp|^2}{B_0^2} (\mathbf{B}_0 \cdot \nabla_0) X \quad (27)$$

The function  $\xi$  which includes the perpendicular description of the leading order displacement is given by the nonlinear ballooning mode envelope equation for tokamak geometries [7, 16]:

$$C_0 \frac{\partial}{\partial \alpha} \frac{\partial^2 \xi}{\partial t^2} + C_5 \frac{\partial}{\partial \alpha} \frac{\partial^2}{\partial t^2} \left[ \int_0^t dt' \frac{\xi(t')}{(t-t')^{\lambda-1}} \right] = C_1 \left[ 2(1-\mu) \frac{\partial}{\partial \alpha} \xi - \frac{\partial^2 \mu}{\partial f'^2} \frac{\partial^2 u}{\partial \psi^2} \right] \quad (28)$$

$$+ C_2 \frac{\partial}{\partial \alpha} \xi^2 + C_3 \left[ \left( \frac{\partial \xi}{\partial \psi} \right)^2 - \frac{\partial^2 u}{\partial \psi^2} \frac{\partial}{\partial \alpha} \xi - \frac{1}{2} \frac{\partial^2 \bar{\xi}^2}{\partial \psi^2} \right] + C_4 \frac{\partial \xi}{\partial \alpha} \frac{\partial^2 \bar{\xi}^2}{\partial \psi^2} \quad (29)$$

where  $\xi = \frac{\partial u}{\partial \alpha}$ , the flux function  $f(\psi)$  can be related to the toroidal field  $B_\phi$  and the major radius  $R$ :  $f = B_\phi R$ .  $\lambda$  is defined as  $\lambda \equiv \sqrt{1 - 4D_M}$  where  $D_M$  is the Mercier coefficient [27]. The coefficients include most of the information of the equilibrium geometry since they are mainly field-line averaged equilibrium quantities. We will investigate the  $C_2$  coefficient in more detail, therefore its expression is provided as a representative example for the coefficients:

$$C_2 = \left\langle \frac{X \hat{P}}{B_0} \right\rangle \quad (30)$$

where the brackets  $\langle \dots \rangle$  denote integrals along the field aligned variable  $\chi$ ;  $\pm p_\chi$  are the limits of these integrals, and:

$$\begin{aligned} \frac{X\widehat{P}}{B_0} &= H [(\mathbf{e}_\perp \cdot \nabla)\mathbf{H}] \cdot (\mathbf{B} \cdot \nabla) [(\mathbf{B} \cdot \nabla)\mathbf{H}] - 1/2H(\mathbf{e}_\perp \cdot \nabla) [\mathbf{H} \cdot (\mathbf{B} \cdot \nabla) [(\mathbf{B} \cdot \nabla)\mathbf{H}]] \\ &+ \frac{1}{2B_0} [(\mathbf{H} \cdot \nabla)\mathbf{H}] \cdot \nabla \alpha \mathbf{e}_\perp \cdot \mathcal{L}(H\mathbf{e}_\perp) + 2(\mathbf{e}_\perp \cdot \boldsymbol{\kappa}_0) \frac{Q_- H}{B^2} \end{aligned} \quad (31)$$

with

$$Q_- \equiv \frac{1}{2} [\mathbf{H}(\mathbf{B} \cdot \nabla) ((\mathbf{B} \cdot \nabla)\mathbf{H}) - |(\mathbf{B} \cdot \nabla)\mathbf{H}|^2] \quad (32)$$

$$\mathbf{H} \equiv \frac{X}{B_0} \mathbf{e}_\perp + G\mathbf{B}_0 \quad (33)$$

where  $\boldsymbol{\kappa}_0$  is the magnetic field curvature and  $\mathcal{L}$  is the linear operator which is defined acting on a perpendicular vector  $\mathbf{W}_\perp$  (with only  $\mathbf{e}_\perp$  and  $\mathbf{e}_\perp$  components) as:

$$\mathcal{L}(\mathbf{W}_\perp) \equiv \mathbf{B}_0 \cdot \nabla_0 [\mathbf{B}_0 \cdot \nabla_0 (\mathbf{W}_\perp)] - (\nabla_0 \boldsymbol{\kappa}_0) \cdot \mathbf{W}_\perp + [\mathbf{B}_0 (\mathbf{B}_0 \cdot \nabla_0) + 2\boldsymbol{\kappa}_0] \left[ \frac{2}{B_0^2} (\boldsymbol{\kappa}_0 \cdot \mathbf{W}_\perp) \right] \quad (34)$$

The nonlinear drive coefficient  $C_2$  has slowly converging integrands as their leading orders are proportional to  $|\chi|^{(2-2\lambda_S)}$ , where  $\lambda_S$  is between 1 and 2. To minimize the numerical calculations we divide the integrals into numerically evaluated regions and remaining integrals at large  $\chi$  which can be evaluated analytically. The coefficients  $C_4$  and  $C_5$  include functions described by differential equations which must therefore be evaluated. The  $C_0$ ,  $C_3$  and  $C_5$  coefficients are only used under certain conditions. The  $C_0$  coefficient must be used if  $\lambda \geq 2$ . If  $\lambda < 2$  we compute and use  $C_5$  instead.  $C_3$  must be determined only if the geometry of the plasma is not up-down symmetric, otherwise it is close to zero. Since we only evaluate up-down symmetric equilibria, this coefficient and its corresponding term are neglected.

### 3.2 MAST coefficient

Here we discuss the results of the coefficients of the original MAST Type I ELM equilibrium and for which we find the following coefficients:

$$C_1 \approx 5.501 \quad C_4 \approx -1.4 \quad (35)$$

$$C_5 \approx 2.878 \quad C_2 \approx -33474 \quad (36)$$

$$\mu \approx 0.74 \quad \lambda \approx 1.252 \quad (37)$$

We notice that both nonlinear coefficients are negative. The negative sign of the nonlinear drive coefficient describes an inwards instead of an outwards explosive drive; but the remaining qualitative behavior of the filaments would be the same as shown in previous work [17, 28]. To show this let's start with the nonlinear ballooning equation implemented in the code Deton8<sup>1</sup> (which is used to solve the nonlinear ballooning equation):

$$D_0 \kappa \frac{\partial^\lambda}{\partial t^\lambda} \xi = \left( D_1 - \frac{(\psi - \psi_0)^2}{\Delta^2} \right) \xi - D_2 \frac{\partial^2 u}{\partial \psi^2} + D_3 (\xi^2 - \bar{\xi}^2) + D_4 \xi \frac{\partial^2 \bar{\xi}^2}{\partial \psi^2} \quad (38)$$

If we transform:  $\alpha \rightarrow a\alpha$ ,  $t \rightarrow \tau t$ ,  $\psi \rightarrow p\psi$  and  $\xi \rightarrow x\xi$  with

$$a = \frac{D_1}{D_2} \sqrt{\frac{D_4}{D_2}} \quad \tau = \sqrt{\frac{D_0 \kappa}{D_1}} \quad (39)$$

$$p = \frac{\sqrt{D_1 D_4}}{D_3} \quad x = \frac{D_1}{D_3} \quad (40)$$

<sup>1</sup>The nonlinear coefficients of Deton8 are related to the nonlinear coefficients of the nonlinear envelope equation as follows:  $D_3 = C_2$  and  $D_4 = C_4$ . To obtain the equation calculated in the code Deton8, we are using the Taylor-expansion of the quantity  $\mu$  and calculating its values numerically. We can set  $C_3 = 0$  since we only analyze up-down-symmetric cases. Furthermore we integrate with respect to  $\alpha$  and exploit that  $\bar{\xi} = 0$ .

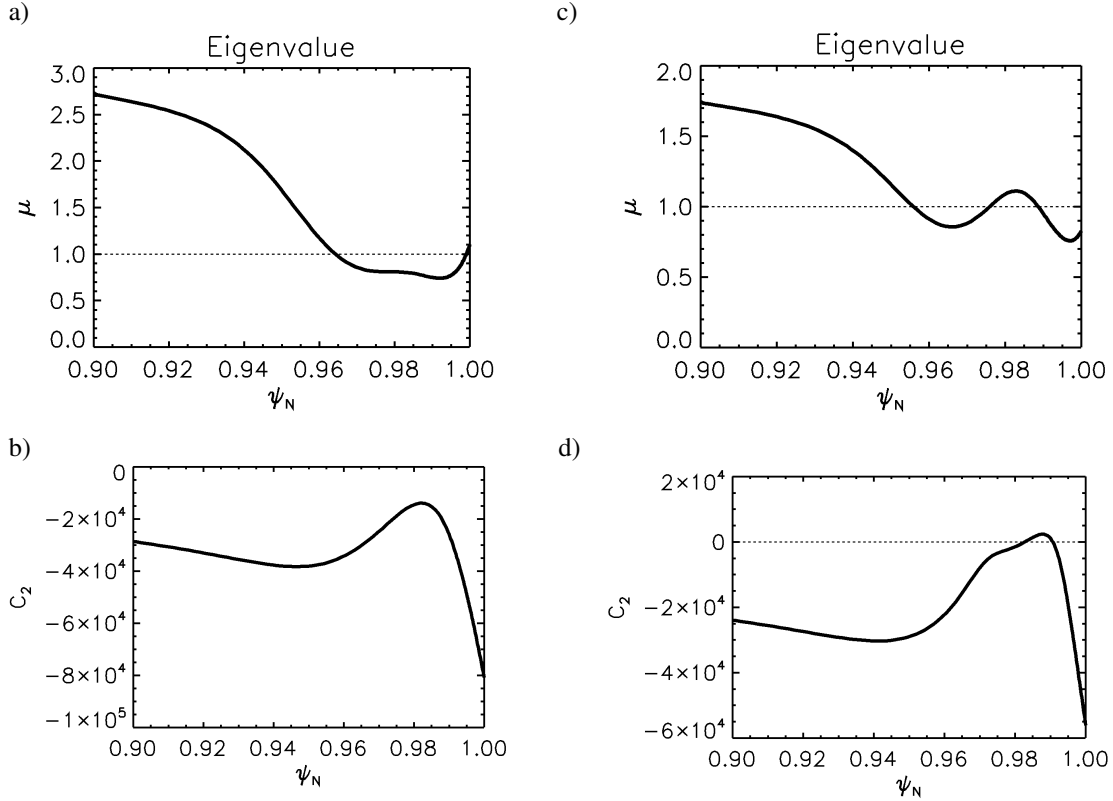


**Fig. 9** Left: Profiles of the coefficients with the original equilibrium. **a)** The original ballooning eigenvalue  $\mu$ . If this value is below 1 the plasma is ballooning unstable. **b)** The original explosive nonlinear drive coefficient  $C_2$ . It continues to be negative. Right: Profiles of the coefficients with an altered equilibrium where the local pressure gradient is increased by 60%. **c)** The altered ballooning eigenvalue  $\mu$ . If this value is below 1 the plasma is ballooning unstable. **d)** The altered explosive nonlinear drive coefficient  $C_2$ . It now has a small but positive value near  $\psi_N = 0.987$ .

and

$$\Delta \rightarrow \sqrt{xp}\Delta \quad (41)$$

we obtain a generic equation where  $\Delta$  is the only parameter. This generic equation was used previously [17, 28] and with it the qualitative results of filaments are similar. If  $D_3$  reverses its sign, the filaments move in the opposite direction, which can be seen by replacing  $\xi \rightarrow -\xi$ . The only term that changes sign by this transformation is the nonlinear drive term. When the sign of the nonlinear drive coefficient is negative, the filament implodes rather than explodes.

However, if the quasilinear nonlinearity coefficient is also negative this leads to an imaginary transformation in the generic equation. This means that the change of this sign leads to a new generic equation. An in-depth discussion of the effect can be found in [16]. Here we concentrate on the nonlinear drive coefficient as it determines the direction of the filament's evolution. Next we investigate if we can find a positive nonlinear drive coefficient to compare this model with ELMs as we know that these have an explosive nature.

### 3.3 Coefficient profiles

The explosive nonlinear drive coefficient is negative for the current Type I ELM MAST case. Therefore the profile of each coefficient relative to the flux surfaces is investigated to determine if the nonlinear drive is negative on all relevant flux surfaces. Additionally we investigate the effects of changing the local pressure gradient on the radial profiles of the coefficients.

The nonlinear ballooning model is valid if the ballooning eigenvalue  $\mu$  is close to but smaller than 1 and if  $\frac{\partial \mu}{\partial \psi} \approx 0$ .  $\mu < 1$  indicates that the plasma is ballooning unstable.  $\frac{\partial \mu}{\partial \psi} \approx 0$  means that  $\mu$  must be a minimum [16]. This means that the values calculated for the coefficients are less precise further away from the extreme of the ballooning eigenvalue.

The ballooning eigenvalue has a broad minimum and differs by around 20% from 1, Fig. 9. Additionally we detect that the nonlinear drive coefficient continues to be negative on all flux-surfaces, but has a local maximum where the plasma is ballooning unstable.

The profiles obtained by increasing the local pressure gradient no longer represent an equilibrium, but help to understand the dependencies of the coefficients. The nonlinear drive coefficient changes if the pressure gradient is adjusted, as illustrated in Fig. 9. Specifically, as the pressure gradient is increased the nonlinear drive coefficient is also increased. Additionally  $\lambda$  exceeds 2 which means that the normal inertial coefficient can be used [7].

Note that for this case there are flux surfaces which are ballooning unstable and have a positive nonlinear ballooning drive, see Fig. 10. However, the local pressure gradient must be changed by 60% in this case. This is larger than we would expect from experimental errors of the pressure gradient measurements which are around 20% [29].

### 3.4 Methods for experimental comparison

We must first identify an appropriate method to compare our results with experimental measurements. The most obvious one is to visualize the results of the simulations and compare these structures with observed structures in experiments. Here we present a method for direct comparison with MAST high speed camera measurements. This method is insufficient for quantitative comparison, therefore a heuristic energy model is presented next. It is used to calculate the energy released in an ELM from the simulated plasma. This energy can be easily compared with energies released in experiments.

We use the coefficients obtained from the case of the increased local pressure gradient, as it is a case which is ballooning unstable with a positive nonlinear drive. However the reader should keep in mind that the equilibrium pressure gradient is increased by 60% which makes the comparison to experiments qualitative, at best. Nevertheless these methods are presented to show that comparison between simulations and experiments is in principle possible.

#### 3.4.1 3D visualization of filamentary structures

To display the perpendicular displacement of the filaments in Cartesian coordinates we first superimpose the solutions of the separated function  $\frac{X}{B_0}$  and  $\hat{\xi}$  given in equation (25), which are the solutions of the linear ballooning equation (26) and the nonlinear ballooning equation (29). The  $\psi$  meshes vary between the two codes (evaluating

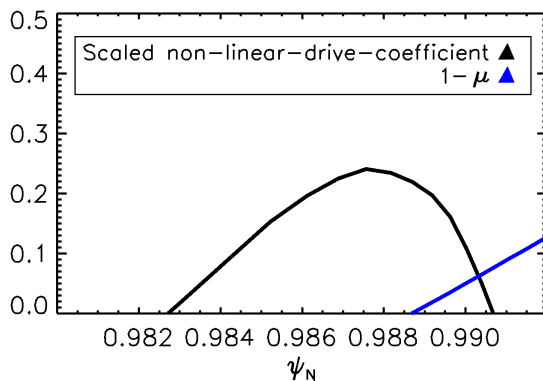


**Fig. 10** Scaled nonlinear drive coefficient and  $1 - \mu$  vs normalized flux surfaces. The plasma is ballooning unstable which means that the linear drive term is initially driving the filaments. Also the nonlinear drive coefficient is positive, which means that it drives the filaments outwards.

the linear and nonlinear ballooning equations), but we only display the displacement from the most unstable flux surface. The next step is to switch from the Clebsch coordinate system to a Cartesian system. We know that the cylindrical coordinate  $\phi$  is related to the Clebsch coordinate  $\alpha$  by the following equation:

$$\alpha = q(\chi - \chi_0) + Y - \phi \quad (42)$$

where  $\chi_0$  is a constant and the periodic function  $Y$  is defined as:

$$Y \equiv \int_0^\chi \nu d\chi - q(\chi - \chi_0) \quad (43)$$

with  $\nu$  defined as  $\nu = \frac{fJ}{R^2}$  and related to the safety factor:  $q = \frac{1}{2\pi} \oint \nu d\chi$  (see [19]).

With this relation we calculate the toroidal angle  $\phi$  for each given  $\alpha$  and  $\chi$ . Furthermore we know the  $Z$  and  $R$  values for each given  $\chi$  as these values are given in the input files for the coefficient code (in the MAST case produced by HELENA). We then exploit the transformation relations for cylindrical coordinates to Cartesian coordinates. A typical result of visualizing the filaments in 3 dimensions with an adjusted mode number<sup>2</sup> is shown in Fig. 11 where the data are depicted on top of a high speed camera image of an H-mode plasma in MAST. The brighter parts are regions with higher values of the displacement. Using this method, we could in principle compare simulations with fast camera observations, as long as the equilibrium used provided suitable coefficients for the nonlinear ballooning mode envelope equation.

### 3.4.2 Heuristic energy model

This model was continued from work presented in Reference [30, 31]. We know that the linear drive in tokamaks is caused by the pressure gradient. The linear drive in our nonlinear ballooning envelope equation (29) is proportional to the ballooning eigenvalue, described by the following relation:

$$1 - \mu = \frac{p' - p'_c}{p'} \quad (44)$$

where  $p'$  is the pressure gradient in the plasma and  $p'_c$  is the critical pressure gradient for instability [32]. In our heuristic energy model we use observations from experiments: first, that the region of the steep pressure gradient

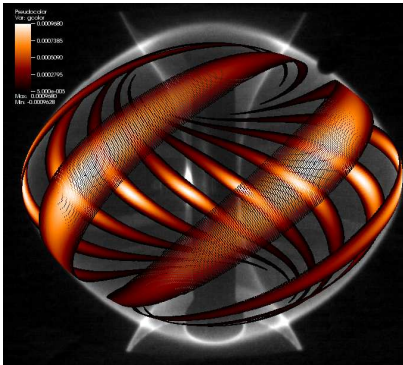


**Fig. 11** 3D structure of the simulated filamentary displacement.

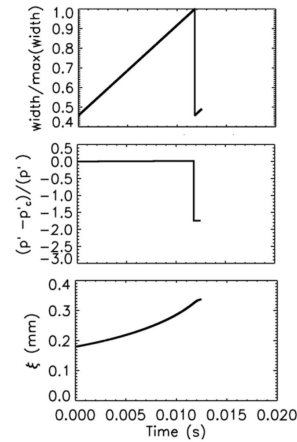


**Fig. 12** Evolution of the normalized width  $\frac{\Delta}{\Delta_{max}}$  of the pedestal (top figure), the evolution of the normalized pressure gradient where the drop of it is seen (middle figure), and the evolution of the displacement (bottom figure). Note, that it is the very beginning of the nonlinear regime where the crash of the pressure gradient is initialized.

<sup>2</sup>The original mode number is reduced by a factor of approximately 20. This high mode number compared to experiments is probably due to the Taylor expansion of the ballooning eigenvalue  $\mu$ . This could be investigated in the future.

(called pedestal) is increasing before an ELM crash and second that the pressure gradient collapses during an ELM crash [32]. Therefore we introduce a pedestal width that grows linearly with time in our model. This is linearly destabilizing, so the perturbation increases until the nonlinear terms are of the same order as the linear terms. Then we make the pressure gradient crash until the instantaneous force on the filaments is approximately zero, see Fig. 12.

To implement this model we must translate it into the correct form to input into our codes. The  $1 - \mu$  is replaced by the Taylor expansion:  $1 - \mu(\psi(0)) - \frac{\partial^2 \mu}{\partial \psi^2} (\psi - \psi_0)^2 = D_1 - \frac{(\psi - \psi_0)^2}{\Delta^2}$ , which allows us to represent the width of the pedestal by  $\Delta$ . To estimate the energy released during the drop in the pressure gradient we make the approximation that the released energy is proportional to the drop in pressure gradient, and the volume of the pedestal. With that we obtain from this heuristic model the energy released in one ELM cycle of  $\sim 0.65$ kJ. Typical energy released during one Type I ELM cycle in MAST are between 0.5-1.7kJ [12, 33].

At this point these values are not predictive. One has to compare several of the calculated energies with experiments since we can adjust several quantities in the model. However it is already promising that it is possible to reach sensible values for the energy released, especially if we consider that there is no kink-drive in our model. This could explain why we had to increase the pressure gradient to find appropriate coefficients. A purely pressure driven ELM is typically a Type II ELM [3, 29] which exists in high collisionality regimes with reduced bootstrap current. Type II ELMs typically release less energy during one ELM cycle, which could explain why the obtained energy is at the lower range of the energies released in MAST.

To evaluate if the missing kink-drive is the explanation for the negative coefficients, the coefficients of a Type II ELM on JET have also be evaluated, but the nonlinear coefficients were also found to be negative [16].

## 4 Conclusion

If not controlled, ELMs are predicted to be a major challenge due to the potential detrimental effects on the plasma facing components in future tokamak devices. Therefore improving the understanding of this type of instability would enhance the feasibility of fusion energy produced by magnetically confined plasmas in tokamaks.

We have presented a promising candidate, the nonlinear ballooning model, to describe ELMs quantitatively since several of its qualitative characteristics of explosive filaments are in agreement with experimental observations of ELMs.

Here we have presented results exploiting this model to investigate first whether the nonlinear interaction of explosive multiple filaments influence their evolution and second whether the nonlinear ballooning model can describe Type I and II ELMs quantitatively. The latter topic is of special interest because the model, once derived, is numerically inexpensive to analyze because one only has to solve two differential equations and therefore could be used for large scans.

In the Sect. 2, we have demonstrated how the interaction between plasma filaments of marginally altered initial amplitudes affects their later evolution by exploiting the nonlinear ballooning mode envelope equation. We showed that the more developed filament grows faster while suppressing the smaller filaments. It is expected therefore, that the filaments which first enter the nonlinear regime will dominate the physics of plasma eruptions. Despite the fact that our results are derived from a slab plasma model, the equation describing the evolution has the same features as in more complex magnetic geometries, including tokamaks [5, 7]. We therefore reason that the phenomenon of large filaments feeding off the smaller ones is a generic feature of ideal MHD. Supporting our model we presented two examples of experimental observations (Type V ELMs in NSTX and ELMs in KSTAR) which show dominant filaments in tokamak geometry where one would expect a higher mode number from linear theory.

This theory is only valid in the early nonlinear stages of the filamentary evolution, and it requires that the dominant filaments will have time to have formed before the model becomes invalid. It is therefore sensible to test these ideas in full, large scale simulations, close to marginal stability.

Recently, it has been shown that there exists equilibrium states with displaced filaments [34]. It remains to be understood how the explosive eruptions evolve to this new saturated state.

In the second part (Sect. 3), we presented that we obtained imploding filaments caused by a negative explosive drive term, but by changing the equilibria we were able to invert the sign. Therefore the results for the ELM equilibria indicate that either the nonlinear ballooning model is not sufficient to describe the explosive nature of

the filaments or that the coefficients themselves are too sensitive to the equilibria, since we can show that they can switch signs depending on the input parameters. Either way the current results suggest that the nonlinear ballooning model alone is insufficient to describe Type I or Type II ELMs quantitatively.

## 5 Acknowledgments

Part of this work is funded by the German National Academic Foundation (Studienstiftung des deutschen Volkes), the German Academic Exchange Service (DAAD - Stipendium für Doktoranden)

I would also like to mention that this work has been carried out within the framework of the EUROfusion Consortium and has received funding from the Euratom research and training programme 2014-2018 under grant agreement No 633053 and from the RCUK Energy Programme (grant number EP/I501045). The views and opinions expressed herein do not necessarily reflect those of the European Commission.

## References

- [1] J. Connor, R. Hastie, H. Wilson, and R. Miller, *Phys. Plasmas* **5**, 2687 (1998).
- [2] J. Connor, *Plasma physics and controlled fusion* **40**(2), 191 (1998).
- [3] P. Snyder, H. Wilson, J. Ferron, L. Lao, A. Leonard, D. Mossessian, M. Murakami, T. Osborne, A. Turnbull, and X. Xu, *Nuclear fusion* **44**(2), 320 (2004).
- [4] H. Wilson, *Fusion Science and Technology* **61**(2T), 122–130 (2012).
- [5] O. Hurricane, B. Fong, and S. Cowley, *Physics of Plasmas* **4**(10), 3565–3580 (1997).
- [6] S. Cowley, H. Wilson, O. Hurricane, and B. Fong, *Control. Fusions* **45**, A31 (2003).
- [7] H. R. Wilson and S. C. Cowley, *Physical Review Letters* **92**(17), 175006 (2004).
- [8] S. Cowley, B. Cowley, S. Henneberg, and H. Wilson **471**(2180), 20140913 (2015).
- [9] S. C. Cowley, B. Cowley, S. A. Henneberg, and H. R. Wilson, arXiv:1411.7797v1 [physics.plasm-ph] (submitted to *Proc. Roy. Soc. A*).
- [10] S. Henneberg, S. Cowley, and H. Wilson, *Plasma Physics and Controlled Fusion* **57**(12), 125010 (2015).
- [11] A. Kirk, T. Eich, A. Herrmann, H. Muller, L. Horton, G. Counsell, M. Price, V. Rohde, V. Bobkov, B. Kurzan et al., *Plasma physics and controlled fusion* **47**(7), 995 (2005).
- [12] A. Kirk, H. Wilson, R. Akers, N. Conway, G. Counsell, S. Cowley, J. Dowling, B. Dudson, A. Field, F. Lott et al., *Plasma physics and controlled fusion* **47**(2), 315 (2005).
- [13] A. Kirk, B. Koch, R. Scannell, H. Wilson, G. Counsell, J. Dowling, A. Herrmann, R. Martin, M. Walsh et al., *Phys. Rev. Lett.* **96**(18), 185001 (2006).
- [14] A. Kirk, H. R. Wilson, G. F. Counsell, R. Akers, E. Arends, S. C. Cowley, J. Dowling, B. Lloyd, M. Price, and M. Walsh, *Phys. Rev. Lett.* **92**(Jun), 245002 (2004).
- [15] H. Wilson, J. Connor, S. Cowley, C. Gimblett, R. Hastie, P. Helander, A. Kirk, S. Saarelma, and P. Snyder, paper TH/4-1Rb (2006).
- [16] S. I. A. Henneberg, *Filamentary plasma eruptions in tokamaks*, PhD thesis, University of York, 2016.
- [17] S. C. Cowley and M. Artun, *Physics Reports* **283**, 185–211 (1997).
- [18] L. D. Landau and E. Lifshitz, *Fluid Mechanics*, 2nd ed. edition (Elsevier Ltd, 2010).
- [19] J. W. Connor, R. J. Hastie, and J. B. Taylor, *Proc. Roy. Soc. A*(365), 1 (1979).
- [20] I. Bronstein, K. Semendjajew, G. Musiol, and H. Mühlig, *Verlag Harri Deutsch* **1** (2008).
- [21] R. Maingi, M. Bell, E. Fredrickson, K. Lee, R. Maqueda, P. Snyder, K. Tritz, S. Zweben, R. Bell, T. M. Biewer et al., *Physics of Plasmas* (1994-present) **13**(9), 092510 (2006).
- [22] G. Yun, W. Lee, M. Choi, J. Lee, H. Park, C. Domier, N. Luhmann Jr, B. Tobias, A. Donné, J. Lee et al., *Physics of Plasmas* (1994-present) **19**(5), 056114 (2012).
- [23] L. Lao, H. S. John, R. Stambaugh, A. Kellman, and W. Pfeiffer, *Nuclear Fusion* **25**(11), 1611 (1985).
- [24] G. Huysmans, J. Goedbloed, and W. Kerner, *Proc. Europhysics 2nd Intern. Conf. on Computational Physics*, 10-14 Sept. 1990 pp. 371–376 (1991).
- [25] C. Konz and R. Zille, *HELENA - Fixed boundary equilibrium solver*, Max-Planck-Institut für Plasmaphysik, Garching, October 2007.
- [26] W. D. D’haeseleer, W. N. Hitchon, J. D. Callen, and J. L. Shohet, *Flux coordinates and magnetic field structure: a guide to a fundamental tool of plasma theory* (Springer Science & Business Media, 2012).
- [27] C. Mercier, *Nuclear Fusion* **1**(1), 47 (1960).
- [28] B. H. Fong, S. C. Cowley, and O. A. Hurricane, *Physical Review Letters* **82**(23), 4651–4654 (1999).
- [29] S. Saarelma, A. Alfier, M. Beurskens, R. Coelho, H. Koslowski, Y. Liang, I. Nunes et al., *Plasma physics and controlled fusion* **51**(3), 035001 (2009).
- [30] S. A. Henneberg, S. C. Cowley, and H. R. Wilson, *European Physical Society, Portugal*, (2015).

- [31] S. A. Henneberg, S. C. Cowley, and H. R. Wilson, European Physical Society, Germany, (2014).
- [32] D. Dickinson, S. Saarelma, R. Scannell, A. Kirk, C. Roach, and H. Wilson, *Plasma physics and controlled fusion* **53**(11), 115010 (2011).
- [33] A. Kirk, G. F. Counsell, G. Cunningham, J. Dowling, M. Dunstan, H. Meyer, M. Price, S. Saarelma, R. Scannell, M. Walsh, H. R. Wilson, and the MAST team, *Plasma Physics and Controlled Fusion* **49**(8), 1259 (2007).
- [34] C. J. Ham, S. C. Cowley, G. Brochard, and H. R. Wilson, *Phys. Rev. Lett.* **116**(Jun), 235001 (2016).